Experimental Mechanics (2024) 64:729–743
https://doi.org/10.1007/s11340-024-01056-y

RESEARCH PAPER

Dynamic Biaxial Compression Tests Using 4 Symmetric Input Hopkinson Bars

P. Quillery[1] · B. Durand[2] · M. Huang[3] · K. Seck[4] · H. Zhao[2,5]

Received: 17 November 2022 / Accepted: 8 March 2024 / Published online: 26 March 2024
© Society for Experimental Mechanics 2024

Abstract

Background Multiaxial dynamic loading situations occur in many industrial cases and multiaxial dynamic test development is thus a crucial issue.

Objective To meet this challenge, a biaxial compression Hopkinson set-up with four symmetric input bars is designed.

Methods The set-up consists of a vertical single striker, a sliding surface mechanism that transfers the impact energy to four horizontal tension bars, and four horizontal Hopkinson bars whose extremities are dynamically compressed by the previous tension bars. Strain gauges on two positions of each Hopkinson bar enable for force and displacement measurements at the bar-sample interfaces.

Results Simple and biaxial compression tests are carried out on cuboid and cross samples, and the sample material dynamic behavior is deduced from simple compression tests.

Conclusions The displacements are also estimated using digital image correlation, which confirms the previous measurements. The consistency of the global sample behavior identified from a biaxial compression test is checked by processing numerical simulations based on the behavior determined in simple compression. The results show that the experimental device can be used to identify any behavior law in dynamic biaxial compression.

Keywords Biaxial compression · Impact testing · Hopkinson bars

Introduction

Multiaxial dynamic test development is a crucial issue because such loading situations occur in common industrial cases such as automotive impacts [1] and high-speed forming or machining [2, 3]. Unfortunately, the very reliable Hopkinson bar test, which enables for accurate measurements at high strain rates, uses the uniaxial compression loading generated by the impact of a projectile. Many devices have thus been designed to perform multiaxial tests from this uniaxial set-up.

A radial pressure can be applied to a cylindrical sample mounted on Hopkinson bars by using a confinement. A vessel can apply a pressure from a fluid, the transverse load is thus easily controlled but remains quasi-static [4]. Inserting the sample inside a rigid tube generates a dynamic radial loading, but the ratio between the radial pressure and the axial stress depends on the sample behavior [5]. Using a perfectly plastic confinement tube makes it possible to maintain a fixed radial pressure [6]. The sample can also be confined with a pre-loaded rigid system, with the same disadvantages as the previous devices [7].

An inclined shear/compression specimen [8] or pressure bars with beveled ends [9] can be used to combine shear and compression. A Hopkinson technique using torsional and compression/tension bars at each side of specimen is also reported [10]. A brake is blocked on the input bar and both compression/tension and torsion are applied on the input boundary of the bar. Then the sudden fracture of the brake generates both torsion and tension/compression waves [11] but the obtained loads are not simultaneous because of the difference between their celerities [12].

In [13], a bulge-test is performed on Hopkinson bars: the external boundary of a circular sheet is in contact with a tubular output bar while the other side of the sheet is submitted to

✉ B. Durand
bastien.durand@ens-paris-saclay.fr

1 Lycée Jean Zay, 63300 Thiers, France

2 Université Paris-Saclay, CentraleSupélec, ENS Paris-Saclay, CNRS, LMPS - Laboratoire de Mécanique Paris-Saclay, 91190 Gif-sur-Yvette, France

3 BYD Auto Co., Ltd., Shenzhen, China

4 KPMG Advisory, Paris, France

5 Sorbonne Universités, UFR 919, 4 Place Jussieu, F-75252 Paris Cedex 05, France

the pressure of a fluid compressed by the input bar. An equi-biaxial tensile state is thus obtained at the center of the sheet. Unfortunately, only sheets can be tested and the displacement field on the sample cannot be easily measured.

Recently, our research team developed a Hopkinson set-up [14] consisting of a single striker, an input bar, an internal output bar and a coaxial external output tube (surrounding the internal bar). The internal output bar generates and measures the axial compression of the cross sample whereas the external output bar generates and measures the transverse compression via a sliding mechanism. This mechanism can be easily adapted to a common compression set-up but it is necessary to determine the friction at the sliding interfaces to well process biaxial tests. Moreover, image correlation is mandatory to obtain the sample displacements because the clearances and intermediate strains in the mechanism do not enable their estimation from bar displacements.

In order to obtain a biaxial dynamic loading frame, two perpendicular Hopkinson bar devices have been also built. In [15], an explosive is used to obtain simultaneous loading waves. The system is rather expensive and difficult to use. Biaxial Hopkinson bar systems using two impactors were reported to generate biaxial compression states on samples [16], but obtaining two simultaneous impacts remains difficult. Recently, a challenge has been met by using four electromagnetic systems which directly load the extremities of four Hopkinson bars [17]. However, such systems remain very expensive. Besides, the bar material must be selected to reduce electromagnetic interferences and a titanium alloy has thus been used.

From the review above, it can be seen that the multiaxial testing design is still a tough issue and that the design of such a test depends on the aimed loading state and on specimens.

This paper focuses on a newly designed Hopkinson device with four symmetric compression bars. By using a mechanism similar as the one used in [14], the impact of a single striker enables for simultaneous loading waves in the bars. The proposed method is validated by testing an aluminum whose three dimensional behavior can be directly extrapolated from the measured behavior in simple compression. The set-up and the measurement processing method are described in "The Set-Up" section. Then, "Experemetal Result" and "Check of the Measurement Consistency Using a Simulation" sections present respectively the raw experimental results and an analysis of a biaxial test based on a numerical simulation.

The Set-Up

Design and Characteristics

The set-up is composed of a single projectile launched by an air gun. By means of a mechanism with sliding parts, the impact generates dynamic loading waves in four orthogonal bar devices which drive the waves towards a cross-shape sample. The arrows in Fig. 1 show the main part motions.

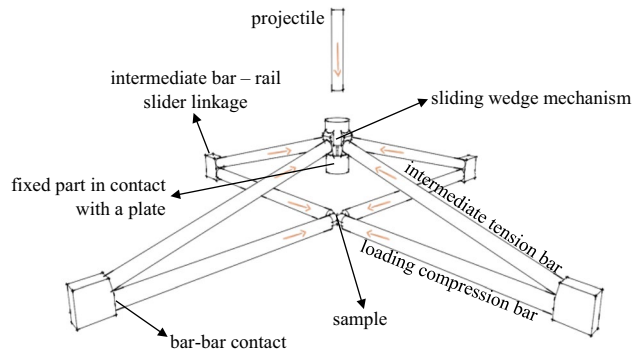

Fig. 1 Scheme of the dynamic biaxial device working (plate and rail not presented here, see also Figs. 2 and 3)

In order to avoid non desired shearing of the sample and to reduce the rigid displacements observed by the camera (below the sample), a symmetric loading configuration has been retained. Below the projectile and the wedge mechanism, the set-up is composed of four identical parts. Each part consists of an intermediate tension bar, linked to a motionless rail by a slider, and in simple contact with a loading compression bar. Because of the slider, the transversal efforts and the bending moments applied by the intermediate bar are absorbed by the rail. Thus, the bar-bar contact transmits only a pure compression along the loading bar (Fig. 4). The intermediate bars are loaded in tension by the projectile impact on the wedge mechanism, and the loading bars are used as input Hopkinson bars to load the sample in compression.

The projectile, launched by an air gun, strikes the mechanism detailed in Fig. 2. The impacted part then moves closer

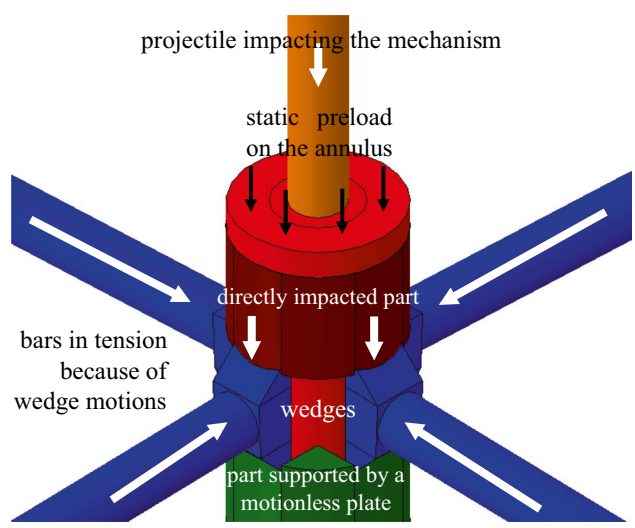

Fig. 2 Sketch of the sliding wedge mechanism

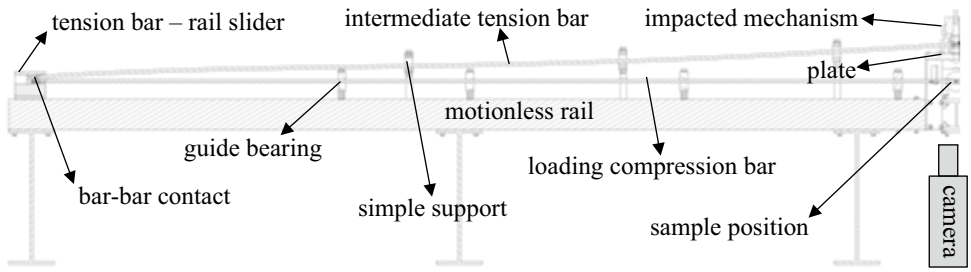

Fig. 3 Drawing of a part of the four Hopkinson bar device (cut-view)

to the supported part, and due to the sliding mechanism, the wedges move towards the center. The bench is Vaseline lubricated and the clearances are suppressed by applying a static preload with a hollow hydraulic actuator (the projectile passing through the hole). It enables for synchronized tension waves in the bars. In order to enable the induced transverse motions, these intermediate bars are not guided by bearings but are simply supported; and they therefore work as cables (Figs. 3 and 29 in the Appendix section). The slider and the bar-bar contact geometry are schematized in Fig. 4. The slider parts are actually linked to the rail (not presented in Fig. 4, see Fig. 3).

A 42CrMo4 steel has been chosen for the bars because of its high elastic limit. Bar lengths are 3 m and their diameters are 10 mm. The wedges and the slider parts are tightened on the bars by standard M6 threads. Two opposite parts can easily be disassembled to use the whole set-up in symmetric simple compression.

The four loading bars are guided by bearings screwed to the rail, exactly as standard Hopkinson bars. Moreover, their extremities are oriented and positioned by the polymer parts shown in Fig. 5. Both symmetric parts (the red and the white ones) are screwed together to enclose the bars. The screw-nut devices are tightened once the four bars are well positioned and well oriented.

All the samples are cut by a waterjet in the same 2 mm thick plate made of AW2024 aluminum. 2 mm × 2 mm × 4 mm cuboid samples are made for simple compression tests and cross samples are made for biaxial compression tests (see Fig. 6 for dimensions). The accurate dimensions of the samples are measured using a caliper before testing them. As shown in Fig. 7 (left), despite its low-cost, the waterjet technique eventually gives a satisfactory geometry. The imperfect shapes that can be seen in Fig. 6 are actually burrs.

During the assembly phase, the camera provides a magnified image of the sample, which enables for a satisfactory positioning of its center with respect to the bar axes. Once the sample is in position, the static preload is applied to fix it.

Instrumentation and Measurements

Axial strain gauges are glued on each of the four loading bars. The classical Hopkinson method usually consists of bonding a gauge at the middle of the input bar and separating the incident wave due to the striker impact and the reflected wave due to the interaction with the sample [4–6, 13, 14, 17–19]. Such a technique is not adapted to our set-up. First, the complex reverberations in the mechanism that convert the projectile impact into four loading waves imply that the incident wave is too long to be distinguished from the reflected one. Moreover, if the loading waves applied on the four Hopkinson bars are not well synchronized, the sample will be first loaded by certain bars, and will then apply a load on the other bars before the arrival of the incident wave at the corresponding interfaces. Such a situation is not foreseen by the classical processing method.

So, instead of a single gauge at the middle of the bars, two gauges are placed close to the boundaries but far enough to be within the Saint-Venant's conditions. Such a method to deal with too long loading waves is reported in the literature [18]. The dimensions are given in Fig. 8 (not on scale). The gauge frequency is 500 kHZ, leading to a $\Delta t = 2$ µs duration between two successive measurements. The celerity C of the one-dimensional waves in the bar steel is determined by measuring the wave propagation time between both gauges, which corresponds to $281 \times \Delta t$. The steel mass density ρ is calculated by weighing

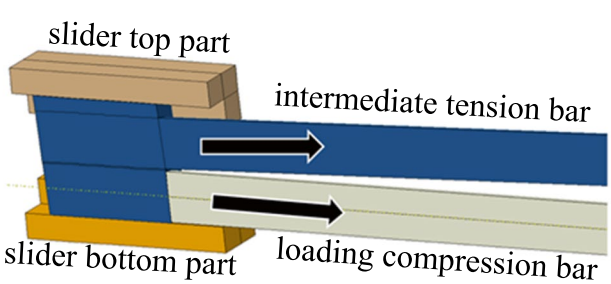

Fig. 4 Schematic cut-view of the slider and of the bar-bar contact (arrows displaying part motions)

Fig. 5 Photograph of the four bar guide (without sample)

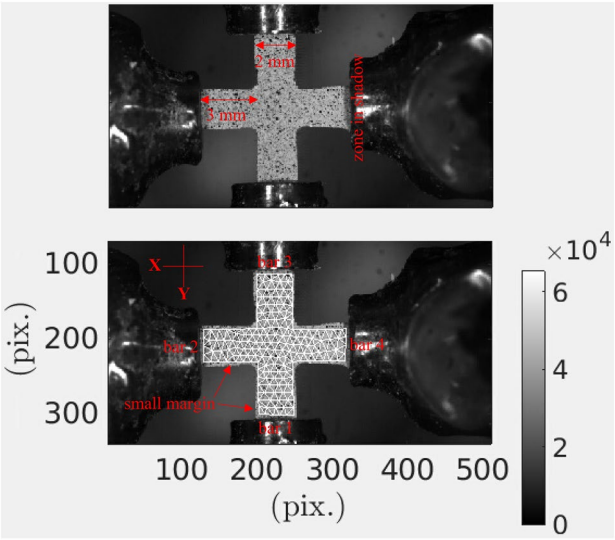

Fig. 6 Reference image of a symmetric cross sample with its initial dimensions (up) and the pixel scale with the grey levels (down)

a cylindrical sample whose dimensions are measured, and the bar Young modulus E and impedance Z are finally estimated by relation (1). The obtained numerical results are given in Table 1.

$$\begin{cases} E = \rho C^2 \\ Z = \rho C \end{cases} \tag{1}$$

The aluminum cross samples are speckled with black paint and observed during the biaxial tests by using an SA5 high-speed camera whose frequency is 50 kHz at a definition of 512 pixels × 272 pixels. Cold powerful lights are necessary to compensate the sensor short integration time; and despite our efforts, a small shadow still remains at the right interface (Fig. 6). The gauge frequency is 10 times higher than the camera frequency. As the two recording devices are started at the same instant, the time-shifting is done knowing that the beginning of the first image and the first strain measurement are synchronized. The very last image before loading is chosen as the reference one and the displacement between each following image and the reference is calculated from Digital Image Correlation (DIC).

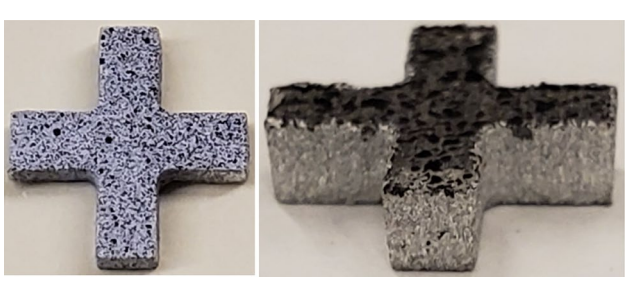

Fig. 7 Photographs of a cross sample, left: top view, right: zoom on the contact faces

DIC is performed by using the in-house Correli RT3 software. The displacement field is defined over a finite-element mesh made of triangular 3-noded elements (T3). The 10 pixel chosen element size leads to the mesh shown in Fig. 6. This mesh accurately follows the sample boundaries by remaining a very small margin. The mean axial displacements on the four interfaces are given in pixels and then converted into millimeters knowing the sample dimensions. In order to obtain consistent kinematic fields, an elastic regularization is used [20, 21]. The relative weight applied to the reference solution corresponds to the fourth power of a regularization length that can be seen as a filtering length. A too high regularization length may lead to erroneous estimations of the experimental displacement field because this field is constrained to be close to an elastically admissible solution. The regulation length has been chosen equal to 10 pixels (as the element size) because it enables for a quick calculation convergence without having any significant influence. Indeed, the projection on a finite-element mesh already filters the displacement field along the element size.

Determination of Forces and Displacements at the Bar-Sample Interfaces from Gauge Measurements

In each bar, both force and displacement time histories can be calculated from the characteristic line method and from the strain evolutions measured by both gauges. First, these strains are converted into stresses by using the Hooke law. Then, the wave propagation phenomenon is studied by using a Lagrange diagram with the axial position x in abscissa and the time t in ordinate (Fig. 9). The stress σ and the particular velocity v can then be calculated at any point by solving the system $\begin{cases} (2) \\ (3) \end{cases}$ representing the conserved quantities along characteristic lines.

$$dt/dx = +1/C \Rightarrow d(\sigma - Zv) = 0 \tag{2}$$

$$dt/dx = -1/C \Rightarrow d(\sigma + Zv) = 0 \tag{3}$$

The bar is initially motionless and preloaded, so the initial conditions are:

$$\forall x, \begin{cases} \sigma(x, t = 0) = \sigma_{ini} \\ v(x, t = 0) = 0 \end{cases} \tag{4}$$

σ_{ini} is the initial stress. Because of uncertainties, the initial stresses given by the gauge measurements are not exactly the same and σ_{ini} corresponds to their mean value. To remain consistent, offsets are actually applied to the measurement histories to bring their initial values to σ_{ini}. The knowledge of the initial conditions makes it possible to determine the velocity at $x = -L$, the left-hand gauge position, from relation (3), and for any instant before L/C. Similarly, the velocity at $x = 0$, the right-hand gauge position,

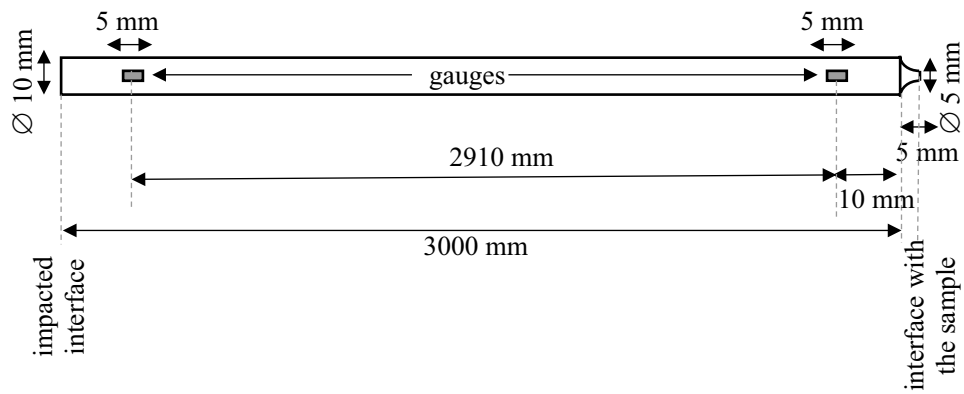

Fig. 8 Sketch of a compression Hopkinson bar instrumented by two axial strain gauges

can be determined from relation (2), and during the same time interval:

$$\forall t \in \left[0, \frac{L}{C}\right], \begin{cases} v(x=-L,t) = \frac{\sigma_{ini}-\sigma(x=-L,t)}{Z} \\ v(x=0,t) = \frac{\sigma(x=0,t)-\sigma_{ini}}{Z} \end{cases} \tag{5}$$

Both stress and velocity being known at the gauge positions during an *L/C* duration, the characteristic line method leads to the following equation system:

$$\forall n \in \mathbb{N}^*, \begin{cases} (\sigma+Zv)\left(x=-L, \frac{L}{C}+n\times\Delta t\right) = (\sigma+Zv)(x=0, n\times\Delta t) \\ (\sigma-Zv)\left(x=0, \frac{L}{C}+n\times\Delta t\right) = (\sigma-Zv)(x=-L, n\times\Delta t) \end{cases} \tag{6}$$

In practice, as the wave propagation duration *L/C* between both gauges corresponds to $281\times\Delta t$, applying the *L/C* time delay merely consists of moving the σ and v evolution vectors along 281 intervals. It is obvious than $\Delta t < L/C$, so with $n=1$, as σ is always measured by the gauges, the unknown v at the gauge positions and at the $L/C+n\times\Delta t$ instant can be determined by solving (6), because both second members have been previously calculated. Then, by successively incrementing n, (6) will always be solvable as second members will have been calculated again from previous resolutions.

Once σ and v calculated at the right-hand gauge position (along the $x=0$ line), these quantities can also be calculated at the sample position (along the $x=l$ line) by using the characteristic line method (Fig. 9) which leads to:

$$\forall t \in \left[\frac{l}{C}, +\infty\right[, \begin{cases} (\sigma-Zv)(x=l,t) = (\sigma-Zv)\left(x=0, t-\frac{l}{C}\right) \\ (\sigma+Zv)(x=l,t) = (\sigma+Zv)\left(x=0, t+\frac{l}{C}\right) \end{cases} \tag{7}$$

Table 1 Mass density, tensile-compressive wave celerity, modulus and impedance of the steel

Density	Wave celerity	Modulus	Impedance
$\rho=7.65\times10^3$ kg.m^{-3}	$C=5.18$ km.s^{-1}	$E=205$ GPa	$Z=39.6$ MPa.m^{-1}.s

Applying the *l/C* time delay consists of moving the σ and v evolution vectors along only a single interval. Eventually, by solving the system (7), one obtains the stress and velocity at the sample interface. The force is merely determined by multiplying the stress by the area of the circular cross-section and the displacement is estimated by a velocity time-integration based on the rectangle method.

Experimental Results

Estimation of the Device Stiffnesses

Bar-bar tests are carried out along both directions, bar 2 in contact with bar 4 for direction X and bar 1 in contact with bar 3 for direction Y (see Figs. 6 and 10). The chosen time origin is different from the "Determination of Forces and Displacements at the Bar-Sample Interfaces from Gauge Measurements" section origin. Indeed, in Fig. 9, the origin is defined as the instant corresponding to the arrival of the wave at left-hand

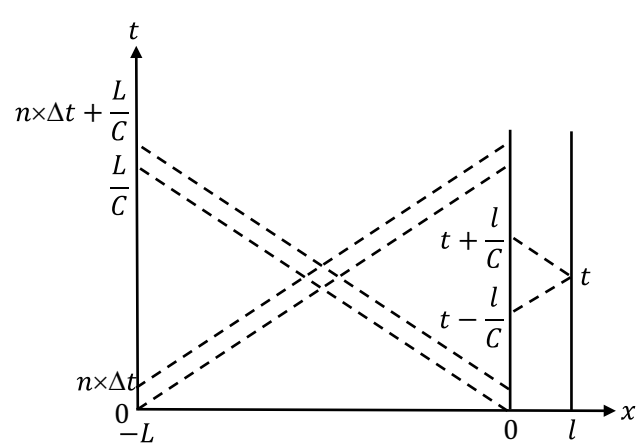

Fig. 9 Lagrange diagram (not on scale), *L* being the distance between both gauges, *l* the distance between the sample interface and the closest gauge, and *n* any positive integer

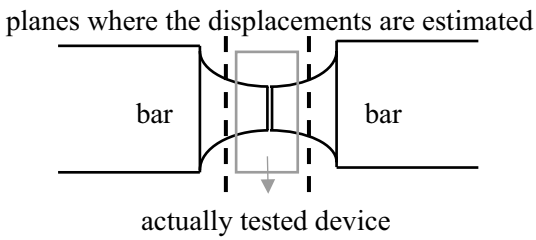

Fig. 10 Schematic of a bar-bar test showing the imperfection of the wave transportation based on the Hopkinson method

gauge position whereas it corresponds to the wave arrival at the sample position in this section. As a good equilibrium can be observed (Fig. 11), the force at the bar contact point is defined as the mean value of the two equilibrated bar forces. The relative displacement between the two bars at the contact point, corresponding to the sum of both bar displacements, is also calculated. The gauge signals are first set to zero before mounting the sample, and a preload is then applied in order to reduce the clearances. At the beginning of the dynamic test, the initial force is thus non-zero. The relative displacements being determined from a time-integration of the velocities during dynamic tests, their zero setting is arbitrary.

Figure 12 displays the force-displacement responses obtained during the bar-bar tests (along Y for the presented examples). A linear evolution can be seen until a 2 kN magnitude, which corresponds to the maximal forces reached on the aluminum samples (see experimental results on "Sample Behavior Identification from a Simple Compression Test" and "Analysis of Biaxial Compression Test Measurements" sections). The displacement zeros are defined to superimpose the linear parts of the curves. For such bar-bar tests, if the gauge signal processing gave the displacements exactly at the interfaces and if these interfaces were perfect, the relative displacement would be zero because of the non-penetration. Here, a linear behavior with a rather reproducible finite stiffness is exhibited. Such a behavior must be due to the one-dimensional assumption which not sufficient to well model the waves close to the contacts. Indeed, the interfaces are not perfect planes but consist of tips whose length is in the same order than the bar diameter and the gauge length, so the estimated displacements

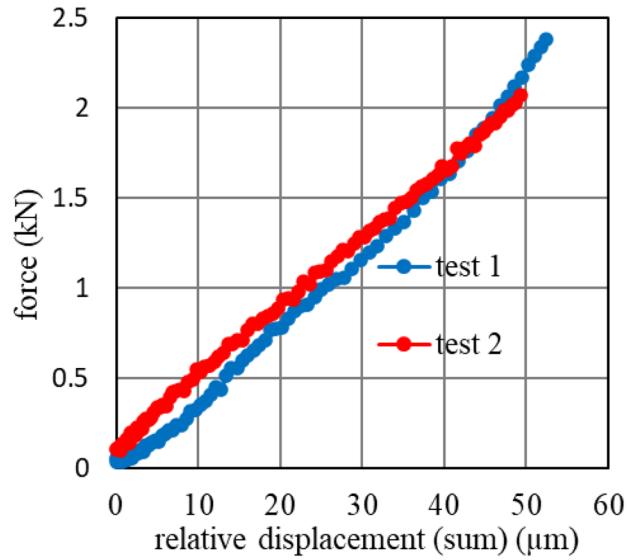

Fig. 12 Force at the contact versus relative displacement (sum of both bar displacements). Curves obtained in the direction Y

are probably a mean value somewhere in the tip. Moreover, as the tip dimension corresponds approximately to the distance covered by the waves during the gauge acquisition time, it is impossible to be more accurate with such a gauge frequency.

The tested device being a small part of the tips in contact (Fig. 10), the corresponding stiffnesses will be called "machine stiffnesses" (i.e. stiffnesses of the machine itself, without any sample). According to the bar-bar tests, 40 kN.mm^{-1} and 28 kN.mm^{-1} values are finally retained, respectively in directions X and Y. In our following test processing, the phenomenon will be taken into account by assuming that opposite interfaces are submitted to the same strain and to the same force, supposed to correspond to the mean value of both opposite forces. Instead of the displacements at the Fig. 10 intermediate planes, it will enable for their estimation at the interfaces.

Sample Behavior Identification from a Simple Compression Test

An aim of the study is to validate the measurements obtained from biaxial tests by checking their consistency with the

Fig. 11 Forces at the bar boundaries in contact during the bar-bar tests, test of the direction Y on left and X on right

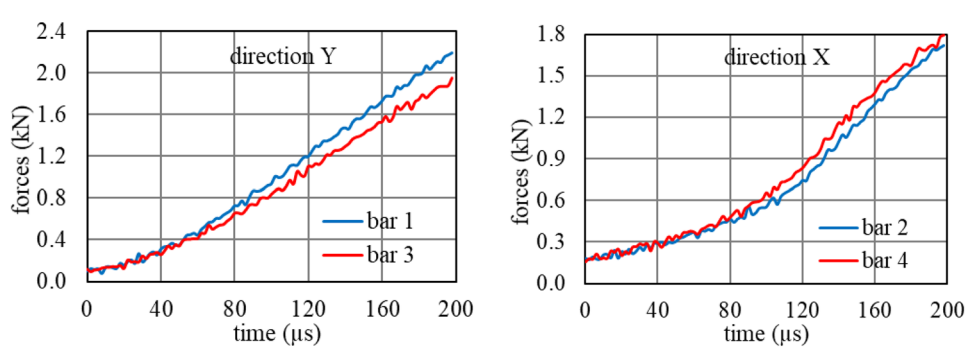

sample behavior. For such performance tests, aluminum has been chosen because its biaxial compression behavior is supposed to be modelled from its simple compression behavior. Indeed, the biaxial behavior can be extrapolated by implanting the uniaxial behavior in a Von-Mises elastic-plastic law with an isotropic hardening. Manufacturers provide a 0.3 Poisson's ratio, so this value will be assumed; but all the other parameters will be measured in order to well model the dynamic compression behavior.

A dynamic simple compression test is carried out on a 2 mm × 2 mm × 4 mm sample, the 2 mm × 2 mm cross-section being the compressed section. The interfaces are Vaseline lubricated to reduce the confinement induced by the lateral friction. The exact dimensions of the sample are measured using a caliper so that the logarithmic strain can be calculated from the estimated interface displacements. The true stress is then calculated from the mean force (the forces being in agreement, see Fig. 13), from the previous strain and from a constant volume assumption. In Fig. 14, the identified Von-Mises behavior is compared to the quasi-static tensile one obtained using a testing machine with a force sensor and an extensometer mounted on a standard sample.

The static tension behavior being determined from standard tests (in two normal directions to check the isotropy), it can be considered to be reliable. Moreover, the measurements lead to typical aluminum characteristics: a 68 GPa Young modulus and a 150 MPa elastic threshold. In its elastic phase, the dynamic compression behavior differs from the reference and seems softer. However, the two plastic parts of the curves match in terms of slope. Taking account of the machine stiffness by removing the interface displacements has almost no influence on the identified behavior, and the elastic slope remains far lower than the reference.

To explain the discrepancy, a relevant explanation lies in a well-known phenomenon in the Hopkinson bar field: an imperfect plane parallelism, occurring even with initially parallel planes because of the "elastic punching" [19].

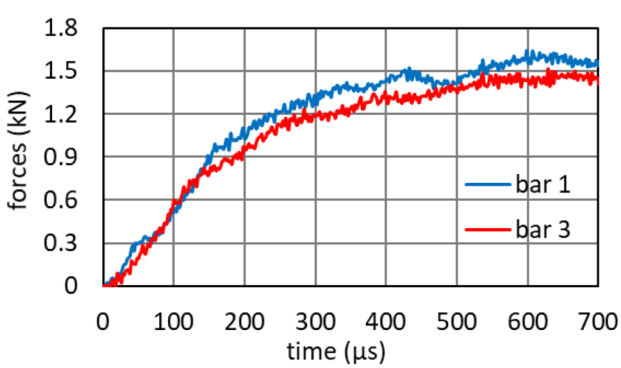

Fig. 13 Comparison of the forces during a simple compression test, processed along X

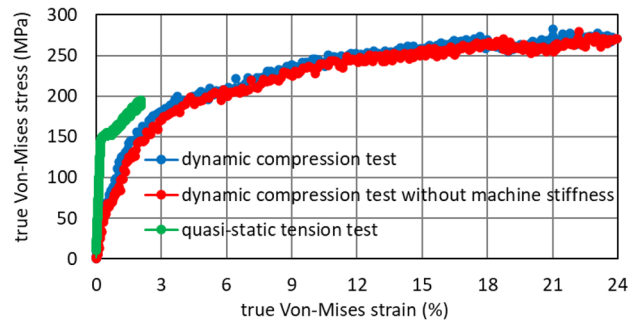

Fig. 14 Comparison of the Von-Mises measured behaviors in static tension and dynamic compression

Because of the high number of samples with different shapes necessary to elaborate the presented study, water jet cutting was the most adapted method to fabricate them. Unfortunately, due to the jet divergence, it induces an imperfection angle (see Fig. 7 (right) and Fig. 15).

This imperfection, as well as usual difficulties to align Hopkinson bars, implies that the short sample length does not enable for Saint-Venant's conditions. There is therefore an axial strain gradient in the order of the elastic threshold, which implies heterogenous plasticity, and thus a decrease of the elastic apparent modulus. That is why the slope of the mean stress – mean strain curve in the apparent elastic phase is thus actually lower than the Young modulus. The strain gradient may be negligible regarding the plastic strains because the plastic parts of the compression and reference curves are in agreement.

Analysis of Biaxial Compression Test Measurements

Seven cross samples made of the previous aluminum are tested using the set-up, still with Vaseline lubricated sample - bar interfaces. The measurements obtained from a test are accurately analyzed to verify their own consistency and the loading paths of the seven tests will be shown. The coherence with the previously measured behavior will be check below (in "Study of the Sample Global Behavior" section).

The measurements of the imposed incident strain waves are analyzed in appendix ("Analysis of the measured incident strain waves" section).

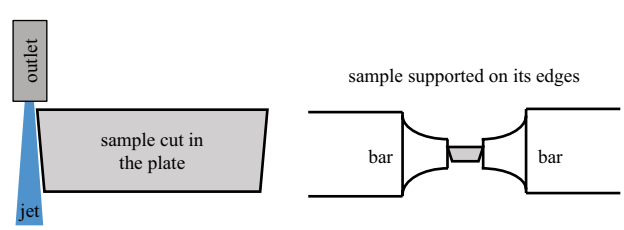

Fig. 15 Imperfect plane parallelism due to the jet (left) and influence on the sample supports (right)

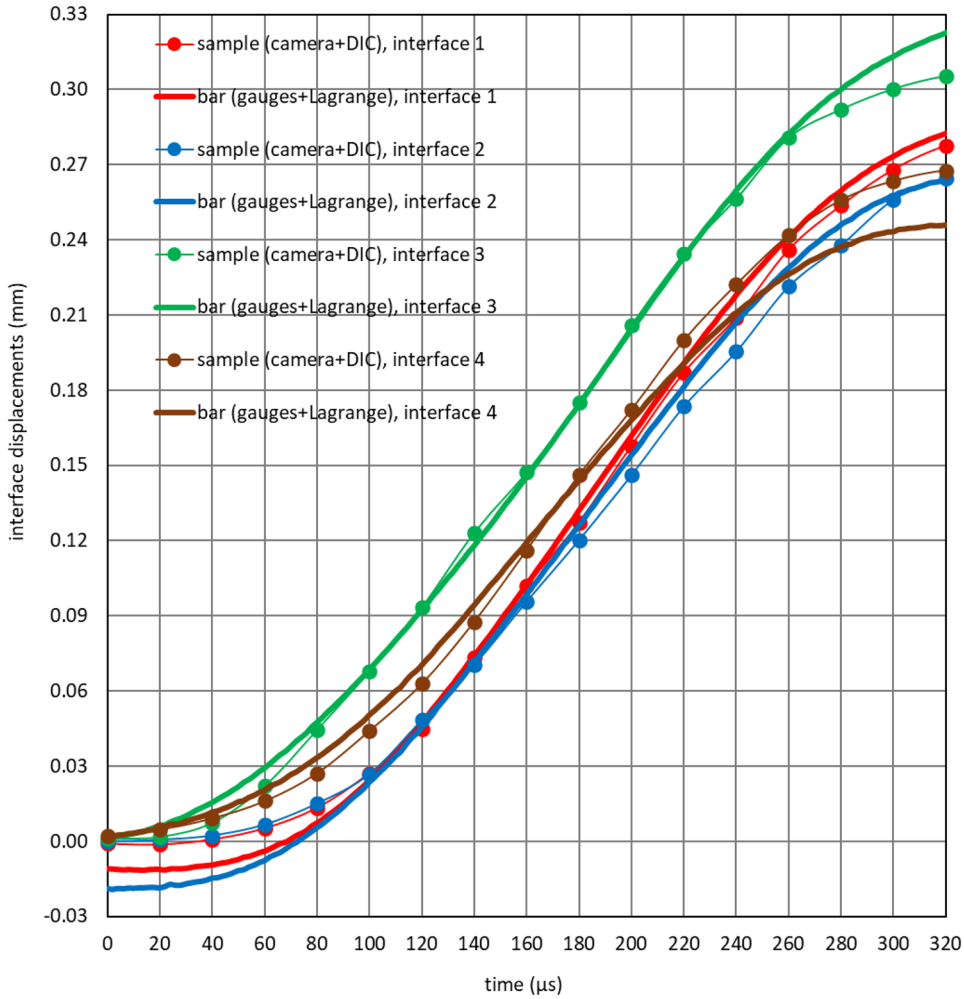

Fig. 16 Comparison of bar (deduced from gauge measurements) and sample (deduced from the images) displacements, oriented towards the center, at the four interfaces (see numbering in Fig. 6)

DIC is processed on the fast camera images to estimate the interface displacements at the mesh middle nodes (Fig. 6). Then, the interface displacements deduced from gauge measurements and those estimated from DIC can be compared:

Figure 16 displays the comparison of results obtained from gauges and from images. While both methods are independent, they match well in the loading phase once the bar curves are shifted using a displacement offset. This offset, which can be observed at the interfaces 1 and 2 (in red and in blue), is actually due to the contact strains. The other discrepancies can be first explained by the relative low frequency of the camera (10 times weaker than the gauge one). Indeed, it can be noted that the time uncertainty is generally lower that the half duration of the image integration (i.e. 10 µs). Although both methods match very well on interfaces 1, 2 and 3 (in red, in blue and in green); a noticeable gap can be seen on interface 4 (in brown). Because

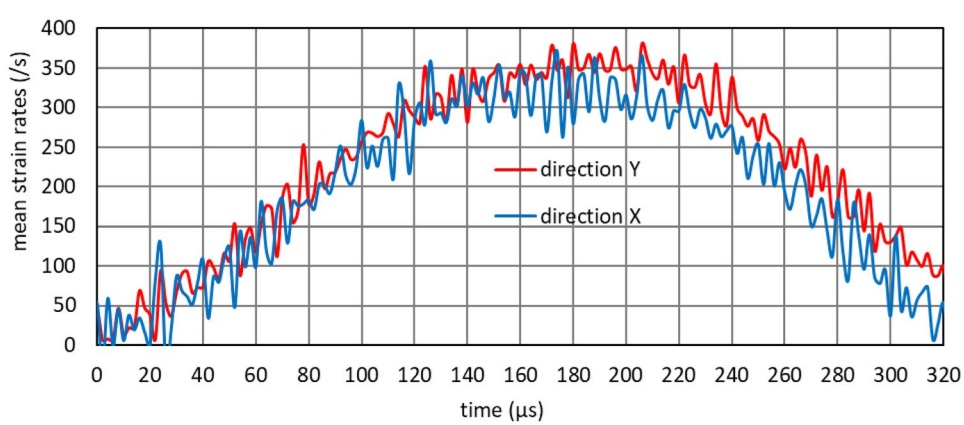

Fig. 17 Time evolutions of the mean engineering strain rates in both directions

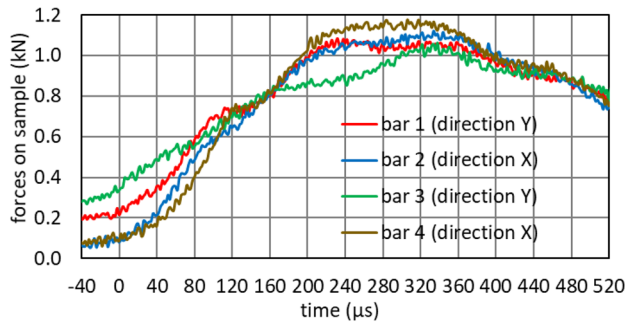

Fig. 18 Comparison of the force histories at the interfaces

of its sign, a first assumption to explain the gap is a contact loss. Moreover, as explained in "Instrumentation and Measurements" section, in spite of our efforts, a small shadow still remains at this interface (Fig. 6) and the lighting may vary with the motion. As DIC is based on the grey level conservation, the so estimated displacement is a bit erroneous. It can also explain the gap.

Figure 16 also compares the displacements deduced from the images at each interface. The dissymmetry that clearly appears can be due to the following imperfections:

- Clearances
- Contact strains
- Frictions
- Defects in the mechanism part geometries

Figure 16 showing very similar results, the strain rates in the sample can be determined from the bar kinematics. As the Lagrange method described in "Determination of Forces and Displacements at the Bar-Sample Interfaces from Gauge Measurements" section directly enables for determination of

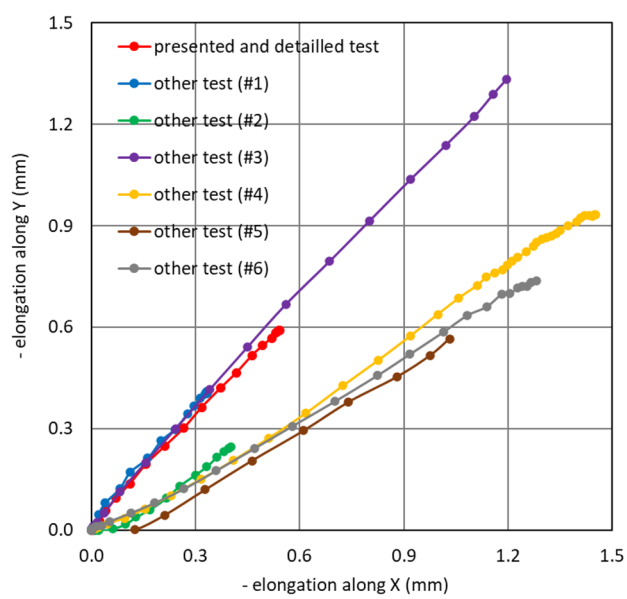

Fig. 19 Loading paths with the (opposite of the) elongations

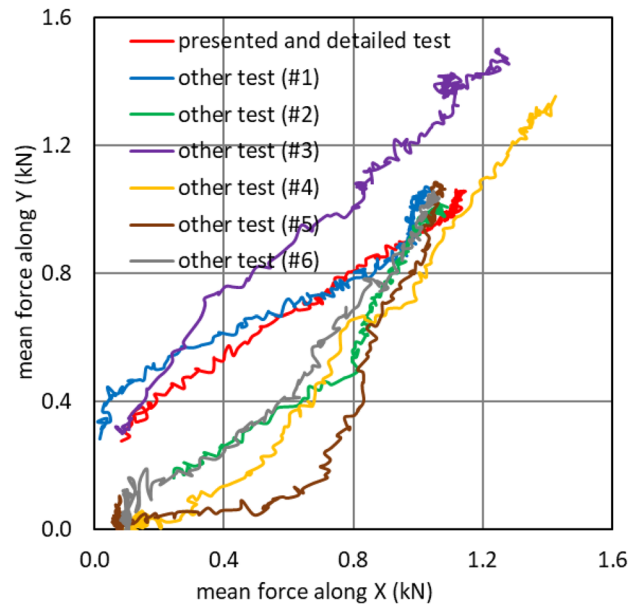

Fig. 20 Loading paths with the forces

the velocities at the bar interfaces, the mean elongation rate in the direction X (respectively Y) can be estimated by summing the bar 2 and bar 4 (respectively 1 and 3) velocities (see Fig. 6). The engineering strain rates are then obtained by dividing the elongation rates by the distance separating opposite interfaces (i.e. 8 mm). According to Fig. 17, it leads to rather linear evolutions of the average strain rates during the loading and the unloading phases with a plateau reaching around 400 s^{-1}.

The force evolutions are shown in the same time basis in Fig. 18. The time origin has been defined as the instant when the velocities at the interfaces rise. In practice, the forces exerted on the sample, initially positive because of the preload, begin to rise slightly before the origin. As it corresponds to the initial elastic phase, the associated displacements are probably too low to be detected. After $t = 320$ µs, the forces decrease and the displacements reach a quasi-steady state, typical of an elastic unloading. While a satisfactory symmetry can be seen along direction X, a

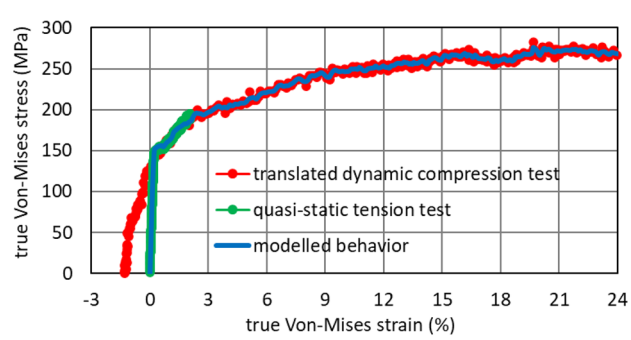

Fig. 21 Von-Mises behavior selected from measurements, in order to implement the numerical model

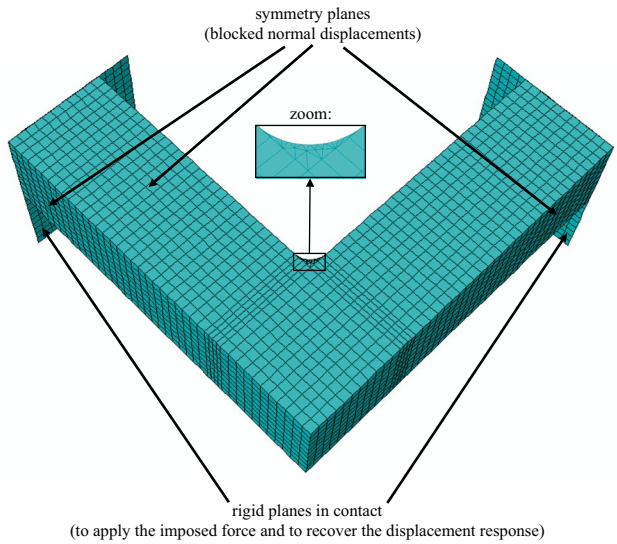

Fig. 22 Sample finite-element modelling (picture extracted from ABAQUS/CAE)

discrepancy can be noted along Y. The discrepancy can be explained by:

- Frictions at the sample interfaces that imply a dissymmetry
- Measurement uncertainties, indeed during bar-bar (Fig. 11) and simple compression (Fig. 13) tests, a gap is observed although no friction can generate a dissymmetry
- A non-equilibrium, but a numerical simulation of the test shows that this assumption is finally not relevant (see "Study of the Sample Equilibrium" section)

The elongation loading paths of the seven tests are presented in Fig. 19 without the unloading phases. The elongations are estimated from the images and from DIC. Except for test #6 for which the regularization length has been increased to 20 pixels, the DIC parameters remain the same. Biaxial (but non perfectly equi-biaxial) paths are exhibited, maybe because of defects in the mechanism. The corresponding force loading paths are shown in Fig. 20. It can be noticed that for each test, the X/Y "disequilibrium" is the same along both elongation and force paths.

Check of the Measurement Consistency Using a Simulation

Assumptions and Parameters

A numerical model of the sample is created to verify the consistency of the experimental results. The finite-element method is implemented in the ABAQUS software, in "Static, General" to model the first preloading step, and then in "Dynamic, Implicit" to model the dynamic step, that corresponds to the test itself. The inertia effects can therefore be analyzed in a rigorous way. The modelled 2 mm thick sample geometry is given in Fig. 6 (up), the radius of curvature at the corners being estimated at 0.2 mm, and the implemented behavior is shown in Fig. 21.

The behavior obtained from the static tension test is chosen as a reference, and as shown in Fig. 21, the behavior retained for modelling first follows the elastic reference until the 150 MPa plastic threshold, and follows then the translated dynamic compression behavior (see also Fig. 14). The beginning of the compression dynamic plastic phase is similar as the static tension one, but for high strains (not shown here) a Portevin – Le Chatelier effect appears in statics and not in dynamics. To model the biaxial dynamic compression behavior, it is therefore relevant to follow the dynamic compression measurements instead of the static tension ones. Indeed, it avoids the plastic behavior discrepancies due to the Portevin – Le Chatelier dynamic effect and due to a possible tension-compression dissymmetry. To sum up, although the raw elastic stress-strain dynamic law

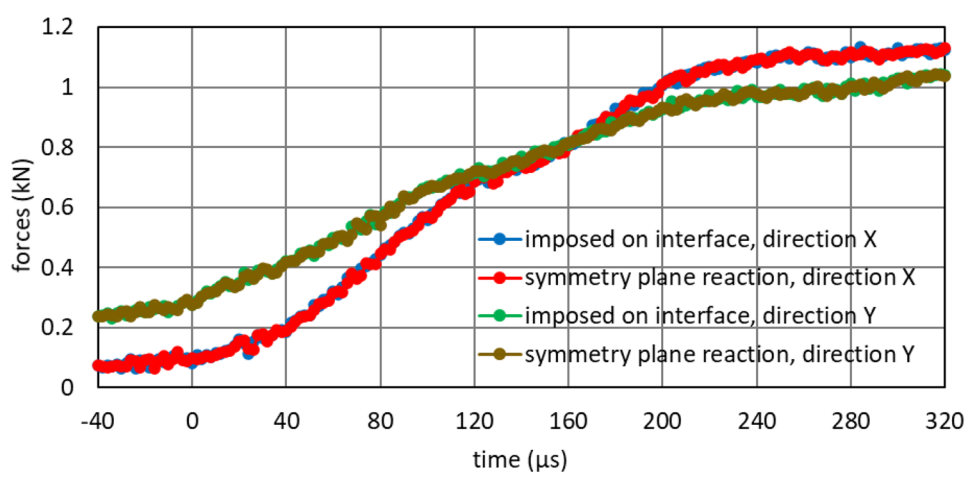

Fig. 23 Time evolutions of the forces at the interfaces and at the opposite planes

is softened, the plastic one should be correct once translated along the strain axis (because the curves agree each other after elastic part). The validity of the described method is proven by a numerical simulation in appendix ("Numerical validation of the identified behavior law" section).

The identified Young modulus, elastic threshold and the constitutive law shown in Fig. 21 are used to define a Von-Mises model with an isotropic hardening. The initial aluminum density is supposed to be 2800 kg.m^{-3}. As the results presented in "Sample Behavior Identification from a Simple Compression Test" section show that the displacements are actually measured with unknown offsets, the calculations are performed by imposing the experimental forces instead of the less reliable experimental displacements.

As Fig. 18 claims for roughly symmetric efforts along the bar directions, the three sample geometric symmetries are also supposed to define loading symmetries (Fig. 22). Only one eighth of the sample is thus modelled and the symmetry planes are blocked to take account of the loading symmetries. Because of these symmetries, the force along a direction is actually defined as the mean value of the two forces in the corresponding bars. As a quarter of each face is represented, the measured forces are divided by four and applied on rigid planes (without inertia) in frictionless contact with the sample interfaces.

The sample mesh is composed of 8 node linear brick elements out of the curvature region, and of 6 node linear triangular prism elements in the curvature region. The rigid plane mesh is composed of 4 node 3 dimensional bilinear rigid quadrilateral elements. The mesh is refined in the curvature region: its size varies from 0.1 mm out of this region to 0.02 mm in the curved edge. That can be seen in Fig. 22. The time increment chosen to process the dynamic step is 2 µs (as the gauge acquisition time).

An explicit solver can also be used, but it must be noted that a very low mass has to be assigned to the rigid planes, otherwise the explicit calculation cannot be performed (a zero mass implying numerical problems). This assigned mass is 1 µg whereas the mass of the modelled sample part is 22.5 mg. The stable increment time necessary to process the calculation with the ABAQUS "Dynamic, Explicit" solver being very low (2.5×10^{-4} µs), using the implicit solver enables for a quicker calculation.

Study of the Sample Equilibrium

The equilibrium can be studied through the previously presented numerical model. First, the static preload is applied by imposing the state at -40 µs in Fig. 18, which corresponds to the beginning of the force increase. Then the measured forces are imposed to process the dynamic simulation until the unloading phase, and the force applied on an interface can be compared to the reaction at the opposite symmetry plane. Figure 23 displays that the modelled sample part is

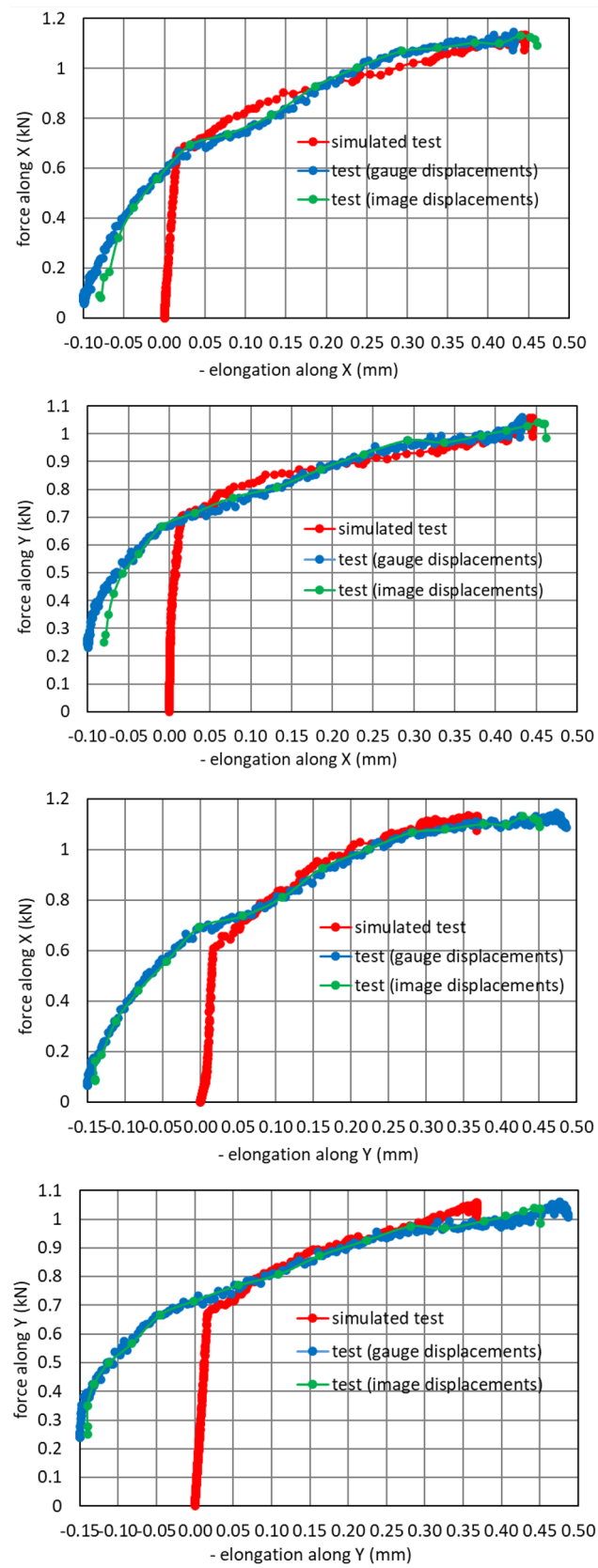

Fig. 24 Forces as functions of the (opposite of the) two elongations for the presented test

perfectly equilibrated during the dynamic test. It confirms that the test has been well designed.

Study of the Sample Global Behavior

The aim of the present section is to check the set-up capacity to identify a constitutive law from a biaxial compression test with the same reliability as from a simple compression test. The simple and biaxial compression samples being made of the same aluminum, the same Von-Mises behavior should be observed.

A relevant criterion to validate our device is the sample global behavior. For such a biaxial compression test, two forces and two elongations are measured in both directions. The experimental force – elongation curves will be compared to their numerical equivalents deduced from the model presented in "Assumptions and Parameters" section. It is reminded that the force in a direction is defined as the mean value of the two corresponding opposite forces, and that the elongation is the opposite of the sum of the two corresponding opposite displacements. The image displacements are not obtained at the same instants as the forces. The force time evolutions, measured in the gauge time basis, are thus interpolated in the image time basis using the Matlab software. In Fig. 24, the force – image elongation curves are then obtained at the image frequency, whereas the force – gauge elongation curves, which do not require any interpolations, are obtained at the gauge frequency.

As explained in "Sample Behavior Identification from a Simple Compression Test" section, because of the non-perfect geometry, the measured apparent elastic slopes are softened. The experimental curves have therefore to be translated along the elongation axes to well match the numerical ones in their plastic phases. However, as explained in "Estimation of the Device Stiffnesses" section, as the forces are initially non-zero, the displacement zero setting is finally arbitrary.

Figure 24 shows that once shifted to take account of the elastic phase uncertainty, the measured plastic behavior is as reliable as the measured behavior taken from a uniaxial test.

Conclusion

The aim was to check the relevance of a new biaxial compression set-up with four perpendicular Hopkinson bars. Each bar boundary is dynamically compressed by the impact of a single projectile, the loading being transferred via a mechanism with sliding surfaces. The tested cross sample, whose total length is 8 mm, is placed at the center of the device, in contact with the bar other boundaries. A preloading system eliminates the initial clearances. The forces and the displacements in the sample are determined using strain measurements from gauges glued on the bars. These displacements are also estimated from high-speed imaging associated with image correlation, and both methods are in agreement. The measurement analysis shows that a rather equilibrated biaxial compression test can be carried out on the aluminum sample, with a strain rate of several hundreds of s^{-1}.

However, the measurement processing also shows that the applied loading is not exactly the same along both directions. But, as these imperfections are measured, the test remains useful to study the sample biaxial behavior. Moreover, the forces applied by two opposite bars on the sample are not always symmetric. In the case of the presented test, the difference can be explained by both interface friction and measurement uncertainty. If the difference was clearly due to friction, it would have been taken into account in the analysis and in the numerical simulation of the test.

Aluminum has been chosen for the sample material because the biaxial compression behavior can be extrapolated from a previous measurement of the simple compression behavior and from a numerical model. The numerical and experimental results match very well during the plastic phase. However, because of the sample short length, which does not enable for a homogenous mechanical state, the elastic properties cannot be identified. This is a common disadvantage of Hopkinson devices in general [19].

This exploratory work can be seen as a calibration of the whole set-up, encompassing the loading device, but also the gauge and camera measurements. An immediate prospect concerns the study of shape memory alloys such as Nickel-Titanium. Indeed, these materials are stain rate dependent [22] and have a plasticity threshold that depends on the stress tensor shape [23, 24].

Appendix

Analysis of the Measured Incident Strain Waves

The strains measured by the gauges next to the impacted interfaces (see Fig. 8) correspond to the incident strain waves in the bars. According to Fig. 8, the distance between these gauges and the sample interfaces is 2910 mm + 10 mm, the incident and the reflected waves are thus separated by a $2 \times (2910\text{mm} + 10\text{mm})/5.18\text{km.s}^{-1} = 1.13\text{ms}$ duration. Figure 25 displays the incident strain wave in each bar in another time-basis. Instant 0 corresponds to the arrival of the incident waves at the gauge positions and the time window is short enough to measure the incident waves not covered by the reflected ones. Figure 25 shows that the whole mechanism between the projectile and the loading

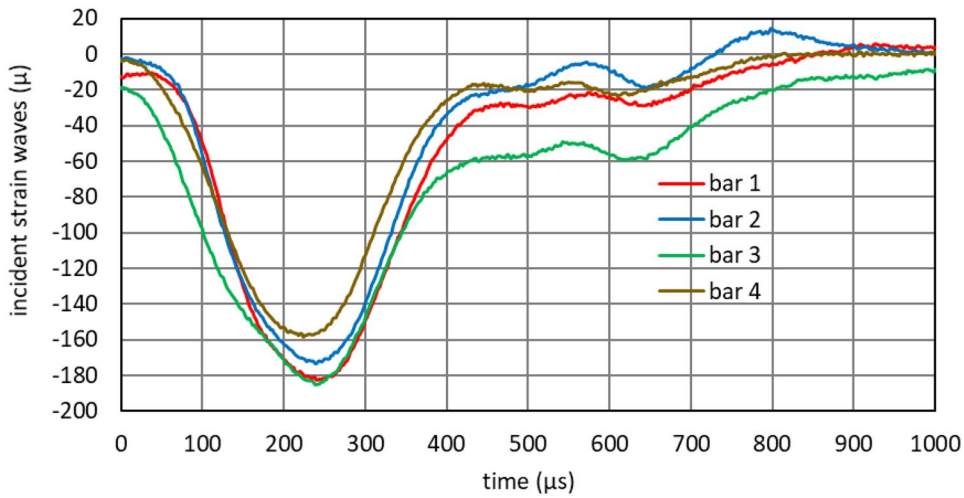

Fig. 25 Incident strain waves in the four bars

compression bars (i.e. the sliding wedge mechanism, the intermediate tension bars and the sliders with bar-bar contacts; see Figs. 1 and 4) modifies the incident wave shapes that do not look like the classical steps. These strain waves, whose shapes are due to the inertias and to the friction at the contacts, then propagate as compression waves along the loading bars.

Numerical Validation of the Identified Behavior Law

A simulation of a uniaxial compression test is performed. The sample material is modelled by using the behavior law described in the second and third paragraphs in "Assumptions and Parameters" section. Under a plane stress and a plane symmetry assumption, only half the sample has to be modelled, the cuboid 2 mm × 2 mm × 4 mm sample is thus reduced to a 2 mm × 2 mm square. The bottom face is in frictionless contact with a motionless rigid body; whereas the top face, inclined by 1° to model imperfections, is in frictionless contact with a rigid body moving from top to bottom:

As the measurements claim for a satisfactory force equilibrium (Fig. 18), the calculation is performed using ABAQUS in "Static, General". 4-node bilinear plane stress quadrilateral elements are used to mesh the sample and 2-D linear rigid link elements are used to mesh the rigid bodies. The sample mesh is shown in Fig. 26.

The homogenized behavior obtained from the numerical force and displacement is then compared to the experimental one and the curves are similar (Fig. 27):

The comparison proves that a default of around 1° can explain the gap between the Young modulus and the measured elastic stress-strain slope. Above all, that proves that the device defaults have no influence on the identified plastic behavior law. Indeed, the modelled plastic phase corresponds to a translation of measurements along the strain axis (as explained at the beginning of "Assumptions and Parameters" section), and the measurements and the simulations are eventually in good agreement.

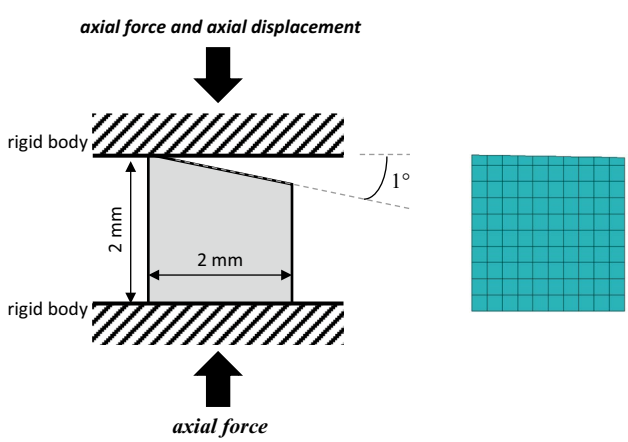

Fig. 26 Simulation of the simple compression test with a 1° imperfection (left) and the finite-element sample mesh (right)

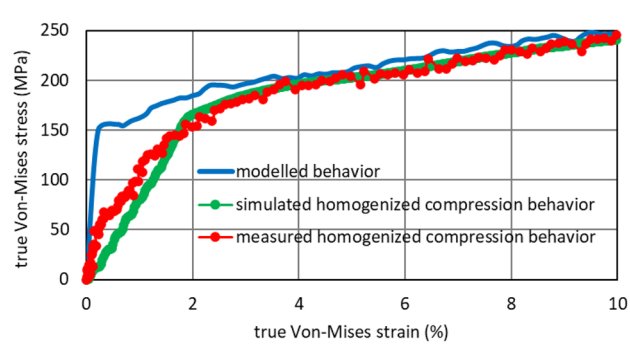

Fig. 27 Comparison between the measured and the numerical compression behaviors

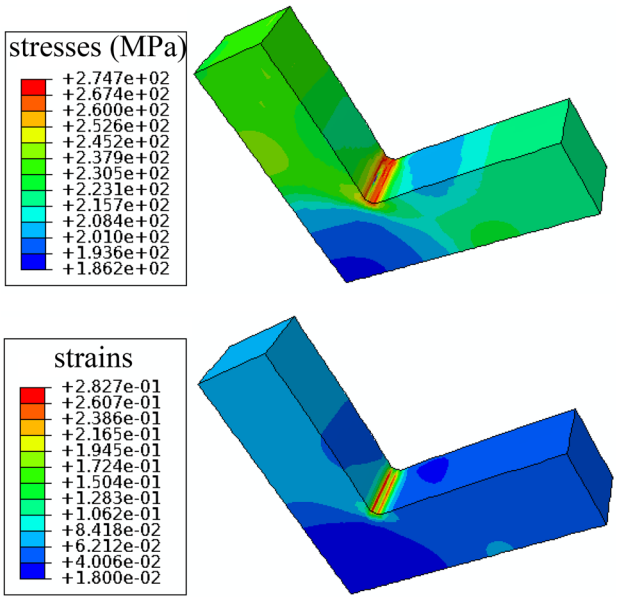

Fig. 28 Von-Mises stresses (up) and Von-Mises equivalent plastic strains (down) inside the deformed sample at the end of the loading phase

State of the Cross Sample at the end of the Biaxial Test

At last, the numerical simulation presented in "Assumptions and Parameters" section enables for estimation of the contours of the Von-Mises stresses and of the Von-Mises equivalent plastic strains inside the deformed cross sample. Figure 28 displays both fields at the end of the loading phase, i.e. at 320 µs in Fig. 23.

Photograph of the Whole Device

Figure 29.

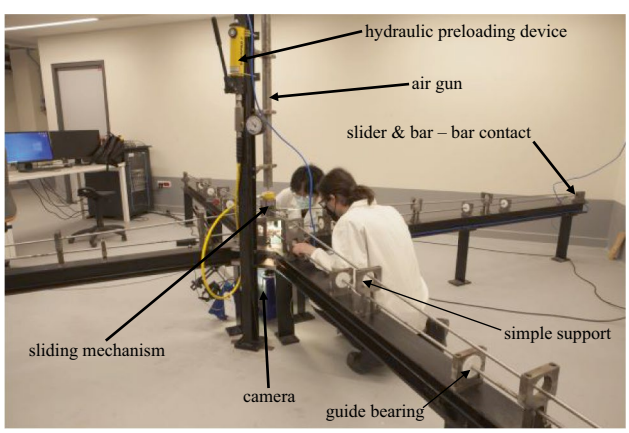

Fig. 29 Real complete device

Acknowledgements The authors thank Y. Barabinot, Z. Du and B. Sauty, Master students, who helped to process the tests.

Declarations

Conflict of Interest The authors declare that they have no conflict of interest.

References

1. Laurent Durrenberger (2007) Analyse de la pré-déformation plastique sur la tenue au crash d'une structure crash-box par approches expérimentale et numérique. Université Paul Verlaine - Metz. Français. ⟨NNT : 2007METZ041S⟩. ⟨tel-01752867⟩
2. Wei Liu (2015) Identification of strainrate dependent hardening sensitivity of metallic sheets under in-plane biaxial loading. Mechanical engineering [physics.class-ph]. INSA de Rennes. English. ⟨NNT : 2015ISAR0005⟩. ⟨tel-01149144⟩
3. Guo Y, Efe M, Moscoso W, Sagapuram D, Trumble KP, Chandrasekar S (2012) Deformation field in large-strain extrusion machining and implications for deformation processing. Scripta Mater 66:235–238
4. Chen W, Song B (2011) Split Hopkinson (Kolsky) Bar. Design, Testing and applications. Springer science & Business Media, LLC. ISSN 0941-5122. ISBN 978-1-4419-7981-0. e-ISBN 978-1-4419-7982-7. https://doi.org/10.1007/978-1-4419-7982-7. Springer New York Dordrecht Heidelberg London
5. Durand B, Delvare F, Bailly P, Picart D (2016) A split Hopkinson pressure bar device to carry out confined friction tests under high pressures. Int J Impact Eng 88:54–60
6. Bailly P, Delvare F, Vial J, Hanus JL, Biessy M, Picart D (2011) Dynamic behavior of an aggregate material at simultaneous high pressure and strain rate: SHPB triaxial tests. Int J Impact Eng 38:73–84
7. Carlo Albertini, Ezio Cadoni, George Solomos (2014) Advances in the Hopkinson bar testing of irradiated/non-irradiated nuclear materials and large specimens. Phil Trans R Soc A 372:20130197. https://doi.org/10.1098/rsta.2013.0197
8. Rittel D, Lee S, Ravichandran G (2002) A shear-compression specimen for large strain testing. Exp Mech 42(1):58–64
9. Hou B, Ono A, Abdennadher S, Pattofatto S, Li YL, Zhao H (2011) Impact behavior of honeycombs under combined shear-compression. Part I: Experiments. International Journal of Solids and Structures 48(5):687–697
10. Lewis JL, Goldsmith W (1973) A biaxial split hopkinson bar for simultaneous torsion and compression. Rev Sci Instrum 44:811–813. https://doi.org/10.1063/1.1686253
11. Stiebler K, Kunze HD, El-Magd E (1991) Description of the flow behavior of a high strength austenitic steel under biaxial loading by a constitutive equation. Nucl Eng Des 127:85–93
12. Philippon S, Voyiadjis GZ, Faure L, Lodygowski A, Rusinek A, Chevrier P, Dossou E (2011) A Device enhancement for the dry sliding friction coefficient measurement between steel 1080 and vascomax with respect to surface roughness changes. Exp Mech 51(3):337–358
13. Grolleau V, Gary G, Mohr D (2008) Biaxial testing of sheet materials at high strain rates using viscoelastic bars. Exp Mech 48:293–306
14. Durand B, Quillery P, Zouari A, Zhao H (2021) Exploratory tests on a biaxial compression hopkinson bar set-up. Exp Mech 61:419–429
15. Albertini C, Montagnani M (1980) Dynamic uniaxial and biaxial stress-strain relationships for austenitic stainless steels. Nucl Eng Des 57:107–123

16. Hummeltenberg A, Curbach M (2012) Entwurf und Aufbau eines zweiaxialen Split-Hopkinson-Bars. Beton- und Stahlbetonbau 107(6):394–400. https://doi.org/10.1002/best.201200013. In German
17. Jin K, Qi L, Kang H, Guo Y, Li Y (2022) A novel technique to measure the biaxial properties of materials at high strain rates by electromagnetic Hopkinson bar system. Int J Impact Eng 167:104286
18. Zhao H, Gary G (1997) A new method for the separation of waves. Application to the SHPB technique for an unlimited duration of measurement. J Mech Phys Solids 45(7):1185–1202. https://doi.org/10.1016/S0022-5096(96)00117-2
19. Safa K, Gary G (2010) Displacement correction for punching at a dynamically loaded bar end. Int J Impact Eng 37:371–384
20. Roux S, Hild F, Leclerc H (2012) Mechanical assistance to DIC. Proceedings of full-field measurements and identification in solid mechanics. F. Hild and H. Espinosa eds., Procedia IUTAM 4, 159–168, Elsevier. https://doi.org/10.1016/j.piutam.2012.05.018
21. Tomicevc Z, Hild F, Roux S (2013) Mechanics-aided digital image correlation. Journal of Strain Analysis 48(5):330–343
22. Dayananda GN, Subba Rao M (2008) Effect of strain rate on properties of superelastic Ni-Ti thin wires. Mater Sci Eng A 486(1):96–103
23. Lexcellent C, Blanc P (2004) Phase transformation yield surface determination for some shape memory alloys. Acta Mater 52(8):2317–2324
24. Maynadier A, Depriester D, Lavernhe-Taillard K, Hubert O (2011) Thermo-mechanical description of phase transformation in Ni-Ti Shape memory alloy. Procedia Eng 10:2208–2213

Publisher's Note Springer Nature remains neutral with regard to jurisdictional claims in published maps and institutional affiliations.

Springer Nature or its licensor (e.g. a society or other partner) holds exclusive rights to this article under a publishing agreement with the author(s) or other rightsholder(s); author self-archiving of the accepted manuscript version of this article is solely governed by the terms of such publishing agreement and applicable law.